Check for updates

Low-Density Multilayer Graphdiyne Film with Excellent Energy Dissipation Capability under Micro-Ballistic Impact

Kailu Xiao, Weiyue Jin, Huibiao Liu, Chenguang Huang, Yuliang Li, and Xianqian Wu*

Dynamical performance of multilayer graphdiyne (MLGDY) with ultra-low density and flexible features is investigated using laser-induced micro-projectile impact testing (LIPIT) and molecular dynamics (MD) simulations. The results reveal that the MLGDY exhibits excellent dynamic energy dissipation ability mainly due to the excellent in-plane wave velocity resulting from the diacetylene linkages between benzene rings. In addition, the unique multiple crack tips and their propagation further promote the energy dissipation capability. The energy dissipation capability of the MLGDY is found to reduce with increasing thickness due to compression-shear induced failure of several upper layers of relatively thick MLGDY, which hinders delocalized energy dissipation ability. Moreover, the impact resistance force of the MLGDY increases almost linearly with increasing impact velocity, demonstrating the applicability of the traditional compressive resistance theory of laminates for MLGDY. Based on the experimental observation and the simulation results, two feasible strategies, i.e., combining with high-strength multi-layer graphene and rotated graphdiyne (GDY) interlayer to avoid stacking of sp-hybridized carbon atoms, are proposed to further improve the impact resistance of the MLGDY. The study provides direct proof of excellent impact resistance of the versatile MLGDY and proposes feasible fabrication strategies to further improve the anti-ballistic performance in future.

1. Introduction

Appeal is growing for 2D carbon materials that exhibit excellent properties, such as good electrocatalytic efficiencies,[1] high

K. Xiao, X. Wu
Institute of Mechanics
Chinese Academy of Sciences
Beijing 100190, China
E-mail: wuxianqian@imech.ac.cn
W. Jin, H. Liu, Y. Li
Institute of Chemistry
Chinese Academy of Sciences
Beijing 100190, China
C. Huang, X. Wu
School of Engineering Science
University of Chinese Academy of Sciences
Beijing 100049, China
C. Huang
Hefei Institutes of Physical Science
Chinese Academy of Sciences
Hefei 230031, China

The ORCID identification number(s) for the author(s) of this article can be found under https://doi.org/10.1002/adfm.202212361.

strengths[2] and thermal conductivities, and extremely low densities, promoting their wide application in the fields of energy storage,[3] coating materials,[4] solar cells,[5] seawater desalination,[6] etc. Graphdiyne (GDY), which is a 2D carbon material with diacetylene linkages ($-C\equiv C-C\equiv C-$), attracts considerable attention in these fields. It exhibits unparalleled advantages in the formation of highly stable interfaces and the protection of high-energy-density electrodes.[7] In addition, its unique nanostructure displays unusual electrocatalytic properties,[8] an excellent photothermal conversion efficiency, and a high synergistic antibacterial activity.[9] Due to such a wide range of applications, dynamic loading due to bubble collapse, dust deposition, and mechanical impact during processing, fabrication, and application may affect the performance of the structure.[10] Therefore, understanding the dynamic responses of GDY films is critical in improving their performances in engineering applications.

Since its first synthesis on a copper surface,[11] the mechanical performance of the GDY film has been critical in terms of expanding its application and further improving its performance. As an allotrope of graphene (GR), the formation of the diacetylene linkages improves the toughness of GDY compared to that of GR, with a slight sacrifice in strength, based on molecular dynamics (MD) simulations.[12] A previous study[13] of the mechanical performances of multilayer GDY (MLGDY) films using atomic force microscopy (AFM) and MD simulations reported the strengths and elastic moduli of the defect-containing films and the stepwise failure behavior of MLGDY under nanoindentation. The dynamic performances of MLGDY films, which is a critical topic with expanding applications, have rarely been directly studied experimentally. Laser-induced microprojectile impact testing (LIPIT) of a multilayer GR (MLGR) film confirmed its excellent specific penetration energy, which is approximately ten times that of steel owing to the ultrafast in-plane elastic wave velocity of 21.07 km s^{-1}.[14] This not only provides an experimental method of studying the impact behaviors of materials at the microscale, but also strengthens confidence in the application of 2D materials in high-efficiency energy dissipation. GDY, with a relatively low density (ρ_{GDY}) of 1.19 g cm^{-3}, still exhibits an elastic modulus (E_{GDY}) and intrinsic strength of 513.8 and 36 GPa, respectively, based on MD simulations.[12b,15]

Hence, the in-plane elastic wave velocity ($C_1 = \sqrt{E_{GDY}/\rho_{GDY}}$) of GDY is ≈20.78 km s^{-1}, which is comparable to that of GR and much higher than those of metals. Currently, related research regarding the failure behavior and efficiency of dynamic energy dissipation of MLGDY is limited to MD simulations, which predict its superior ductility due to the introduced extended acetylenic bonds. These bonds may not only dissipate the kinetic energy of a projectile via in-plane wave propagation and deformation, but also slowly extend the acceleration time of GDY films during contact with projectiles.[16] The lack of direct experimental studies of the impact responses of MLGDY films limits their application in the field of impact protection due to the relatively large differences between experimentally prepared GDY and that simulated using MD.

In this study, the impact responses of MLGDY films with various thicknesses were measured directly using LIPIT, and the underlying thickness-dependent mechanisms of dynamic energy dissipation were investigated using MD simulations. The overall aims of this study are to provide experimental evidence of the excellent impact resistances of MLGDY films, elucidate the relationship between the microstructure and impact resistance of the MLGDY film, and reveal the corresponding thickness-dependent dynamic responses of the MLGDY film. This study not only provides insight into the dynamic behaviors of MLGDY films, but also broadens the applications of MLGDY in the field of impact protection as an extraordinary bulletproof material.

2. Results and Discussion

2.1. Characteristics of the MLGDY Film

The 2D MLGDY nanosheets with wrinkling characteristics (**Figure 1**a), as observed using scanning electron microscopy (SEM), are formed on the surface of copper foil (see Experimental Section and Figure S1, Supporting Information). The enlarged red-dotted rectangular region shown in Figure 1a reveals the unique surface of the MLGDY film with erect nanowalls and uniformly distributed voids of tens to hundreds of nanometers. These voids, which are critical in energy dissipation, endow the MLGDY film with the properties of 3D porous materials with network structures. The inset high-resolution transmission electron microscopy (HRTEM) image of MLGDY reveals an interlayer spacing of 0.365 nm. In addition, the 2D morphology of the MLGDY film (Figure 1b), as determined using AFM, indicates that the surface of the prepared sample displays excellent smoothness and quality, ensuring the consistency of the dynamic performance during LIPIT. The surface roughness of the prepared MLGDY with a thickness of 500 nm is about tens of nanometers (Figure 1b).

To identify the structure and elemental composition of the MLGDY sample, three positions of the produced MLGDY film were randomly subjected to Raman spectroscopy. The Raman spectra display four peaks at 1386.7, 1572.4, 1926.4, and 2190.2 cm^{-1} (Figure 1c), and the wavenumbers of the peaks are consistent at the three selected positions. The intense peaks at 1386.7 and 1572.4 cm^{-1} are due to the breathing and E$_{2g}$ in-phase stretching vibrations, respectively, of sp^2-hybridized

carbon within the aromatic rings. The intensity ratio of these peaks is 0.79, indicating that the MLGDY film exhibits a highly ordered structure and a low number of defects. The peaks at 1926.4 and 2190.2 cm^{-1} are attributed to the vibrations of the conjugated diyne linkages (−C≡C−C≡C−). The results of a narrow scan of the MLGDY film for asymmetric C 1s using X-ray photoelectron spectroscopy (XPS) are deconvoluted into four sub-peaks at 288.2, 286.9, 284.1, and 285.1 eV (Figure 1d). These peaks represent the C 1s orbitals of C−O, C−O, C−C (sp), and C−C (sp^2), respectively, as determined after deducting the Shirley background and fitting via a combination of Lorentzian and Gaussian functions.[17] The XPS and Raman spectra of the MLGR film are shown in the Supporting Information (Figure S2).

The LIPIT platform was used to initiate a high-impact-velocity (V_i) microprojectile to impact the MLGDY film after it was transferred to a 100 mesh copper TEM grid (hole size: 160 × 160 μm, Figure 1e), and a high-speed camera was used to capture the real-time trajectory of the microprojectile. The thicknesses of the 30 ± 0.4 nm MLGDY films were measured via AFM (Figure 1f), whereas those of the 500 ± 20 nm and 2 ± 0.04 μm MLGDY films on the copper foil were measured using focused ion beam SEM (FIB-SEM, Figure 1g,h).

2.2. Ballistic Resistance of the MLGDY Film

To evaluate the ballistic resistance of the MLGDY film under microprojectile impact, a silica projectile with a diameter of 25 μm (**Figure 2**a) was employed and launched with velocities of 280–500 m s^{-1} by varying the energy of the ablation laser. The entire impact process was recorded in fast multi-exposure images (Figure 2a), wherein the motion of the microprojectile may be distinguished. The projectile velocities before and after impact were calculated by measuring the distance traveled between the continuous snapshots of the projectile divided by the time between consecutive images. To accurately obtain the reduction in the kinetic energy (ΔE_a) of the projectile, the effect of projectile attenuation due to air drag[18] was considered, and ΔE_a was corrected (see Figure S4, Supporting Information).

Notably, the evaluated MLGDY films were fully perforated using the adjusted V_i due to the relatively large mass of the projectile used. Based on the relationship between the post-penetration residual velocity (V_r) and V_i of the projectile (Figure 2b), V_r decreases with an increase in the thickness of the MLGDY film at the same V_i, indicating that higher absolute impact energy may be dissipated by a thicker MLGDY film. Moreover, the absorption energy (E_p) of the target material during penetration is calculated using ΔE_a of the projectile: $E_p = \Delta E_a = \frac{1}{2}m_p(V_i^2 - V_r^2)$, where m_p represents the mass of the projectile. E_p depends on the energy dissipation channels of the target materials, including elastic and plastic deformation and crack propagation. The relationship between ΔE_a and V_i (Figure 2b) is obtained based on the relationship between V_r and V_i, which directly reveals an increase in the absolute energy absorption with an increase in the thickness of the MLGDY film. To quantitatively compare the ballistic resistances of different materials with various thicknesses and projectile
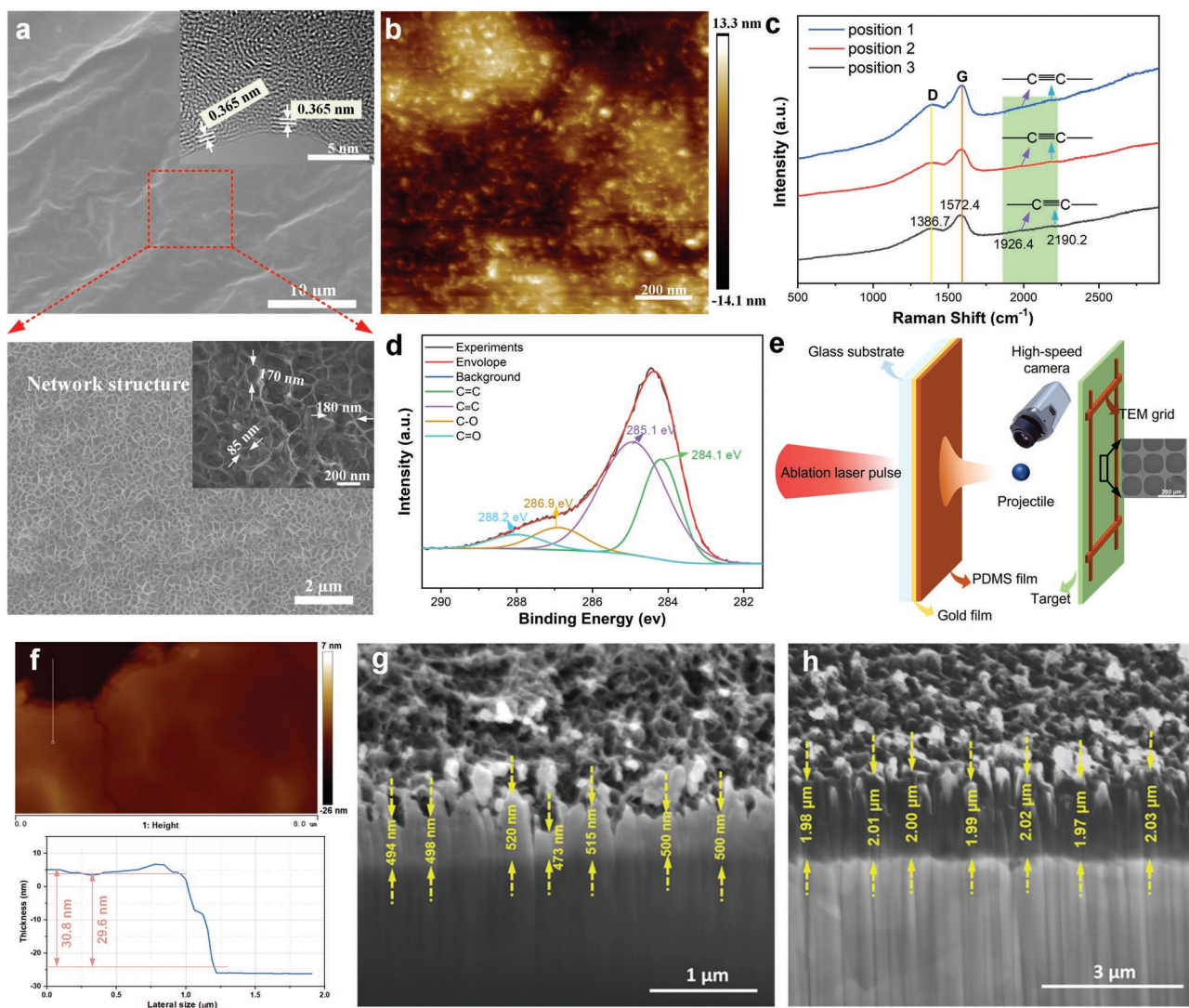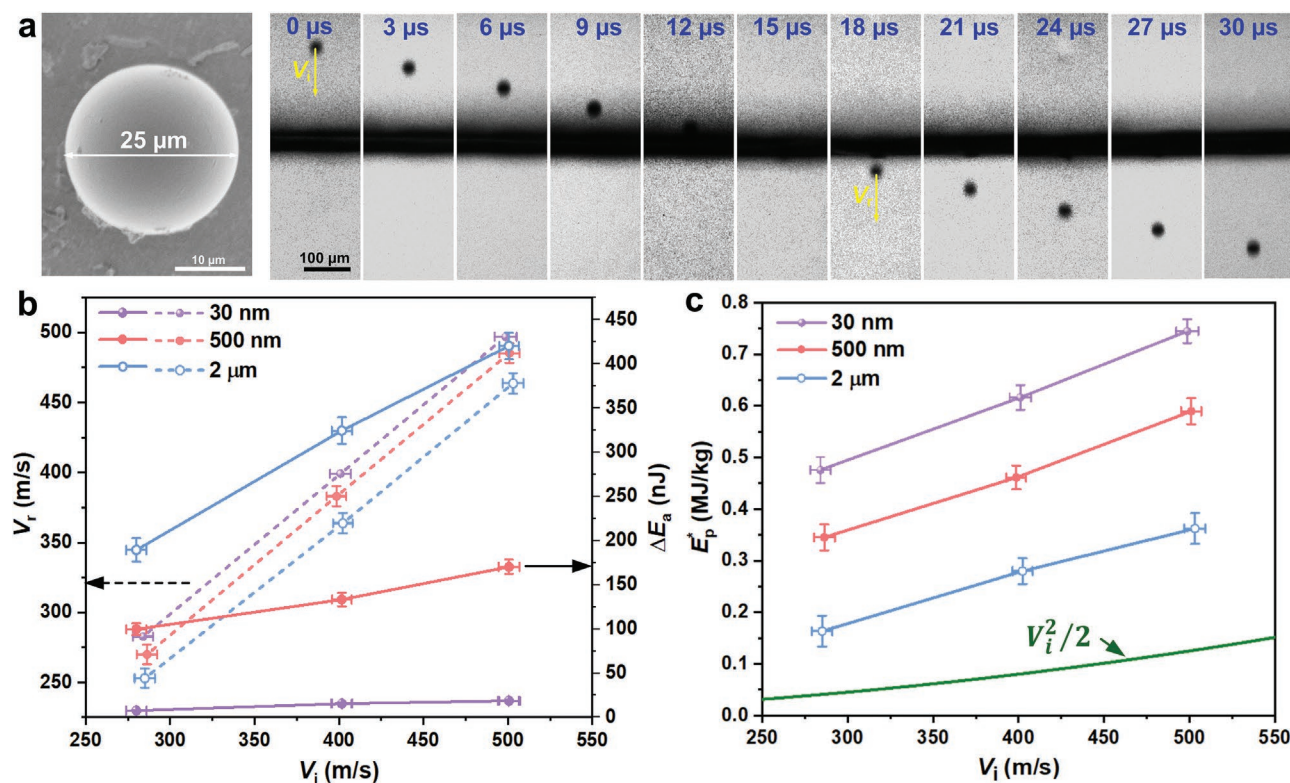
Figure 1. a) SEM image of the MLGDY film and the corresponding network structure, as indicated by the enlarged red-dotted rectangle, and the HRTEM image showing the interlayer spacing of 0.365 nm. b) AFM surface morphology image of the MLGDY film, indicating a well-defined surface. c) Raman spectra of the MLGDY film, which are very consistent at three different positions. d) Narrow scan of the GDY film for asymmetric C 1s using XPS, with the four sub-peaks at 288.2, 286.9, 284.1, and 285.1 eV representing the C 1s orbitals of C=O, C−O, C−C (sp), and C−C (sp^2), respectively. e) Schematic diagram of the experimental platform for LIPIT and the imaging process. Thickness measurements of the f) 30 ± 0.4 nm MLGDY film via AFM and the g) 500 ± 20 nm and h) 2 ± 0.04 µm MLGDY films via FIB-SEM.

masses, the specific penetration energy (E_p^*) is defined by the absorption energy normalized by the mass of the target material in the impact region (m_s):[14,19] $E_p^* = E_p / m_s = E_p / \rho A_s h$, where ρ, A_s, and h represent the density, area of the impact region, and thickness of the target material, respectively.

The E_p^* of the MLGDY film is a function of V_i (Figure 2c), where the green $V_i^2/2$ curve indicates the baseline of E_p^*. As V_i increases, E_p^* increases, and the E_p^* of the MLGDY film increases with decreasing thickness, which may be ascribed to the changes in the failure modes and energy dissipation channels. The MLGDY films with thicknesses of 30 nm exhibit the highest E_p^* of 0.74 ± 0.034 MJ kg^{-1} at 500 m s^{-1}, which is ≈32% and ≈124% higher than those of the MLGDY films with thicknesses of 500 nm or 2 µm, respectively. Meanwhile, the MLGR films with thicknesses of 500 nm were also evaluated

(Figure S5, Supporting Information) to provide a quantitative comparison with the results obtained using the MLGDY film, and the E_p^* of the MLGR film is consistent with that reported by Lee et al.[14] The strength (≈36 GPa), elastic modulus (≈513 GPa),[15] and density (1.19 g cm^{-3}) of GDY are only 33–50% of those of the GR film, with a strength, elastic modulus, and density of 130 GPa, 1 TPa, and 2.21 g cm^{-3},[12b,20] respectively. This is due to the formation of the diacetylene linkages between the benzene rings. Remarkably, however, the E_p^* of the MLGDY film may be up to 87% of that of the MLGR film at the same thickness. This provides more confidence in using such a lightweight 2D material in designing flexible, ultralight energy dissipation materials and structures. Unlike those of polymer materials, such as polystyrene[18], poly(vinylidene fluoride-*co*-trifluoroethylene)[21] and polycarbonate films,[22] impact-induced

**ADVANCED
SCIENCE NEWS**

www.advancedsciencenews.com

**ADVANCED
FUNCTIONAL
MATERIALS**

www.afm-journal.de

Figure 2. a) SEM image of a silica projectile with a diameter of 25 μm, which was used in LIPIT. And the impact was recorded using a high-speed camera, which allows to track the motion and displacement of the projectile. b) Residual velocity (V_r) and change in kinetic energy (ΔE_a) of the projectile. c) Specific penetration energies (E_p^*) of the MLGDY films with different thicknesses. The in-plane sizes of the MLGDY samples used in LIPIT are 160×160 μm.

adiabatic heating and the corresponding nonlinear viscoplastic deformation dominate the energy dissipation process. The increase in temperature upon energy dissipation is insignificant in MLGDY and MLGR owing to their high melting temperatures, and the ultrafast in-plane wave propagation considerably promotes energy dissipation.

2.3. Thickness-Dependent Failure Morphologies

The post-mortem morphologies of the MLGDY films with different thicknesses (**Figure 3**) under various impact velocities were investigated to determine their failure characteristics and energy dissipation mechanisms. During impact, a compressive stress wave is generated in the MLGDY film and propagates back and forth in the thickness direction, leading to a rapid stress equilibrium in this direction. Meanwhile, a radial longitudinal stress wave is generated and propagates within the film, followed by conical deformation and radial crack propagation, leading to the final failure morphologies of the MLGDY films, as shown in Figure 3. Therefore, the principal energy dissipation channels consist of the propagation of the radial longitudinal stress wave at a speed of 20.78 km s^{-1}, conical deformation at a speed of 4 km s^{-1}, and crack propagation. These energy dissipation channels depend strongly on the thickness of the film and the V_i of the projectile.

In the MLGDY film with a thickness of 30 nm at a V_i of 280 m s^{-1} (Figure 3a-i), a semi-annular crack with a zigzag boundary is initially formed in the impact region because of increased tensile stress at the periphery during impact. Subsequently, a radial crack is initiated and propagates along the upper right direction perpendicular to the semi-annular crack. Simultaneously, the tips of the semi-annular crack propagate along the direction of the most severe shear deformation, and a perforation hole is formed during the tearing of the petal. During the dynamic bending of the petals, creases also formed (as indicated by the pink arrow). With increasing V_i (Figure 3a-ii,-iii; Figure S6a, Supporting Information), a clear curling of the petal is observed due to the release of the stress wave as the crack propagates. The degree of curling is enhanced with an increase in V_i, which is characteristic of the thin film. The irregular perforation area (S_p) increases with an increase in V_i (Figure S7, Supporting Information) because a larger area is affected by an impact with a higher V_i. The results of SEM indicate that, in addition to the stress wave propagation, the initiation and propagation of the semi-annular and radial cracks, the tearing of the petals, and the creasing and curling of the film with a thickness of 30 nm contribute to the dynamic energy dissipation.

Similar curling behaviors (as indicated by the yellow arrow) of the petals are also observed, to reduced degrees, in the films with thicknesses of 500 nm (Figure 3b). In addition to the semi-annular cracks, more crack branches are generated around the
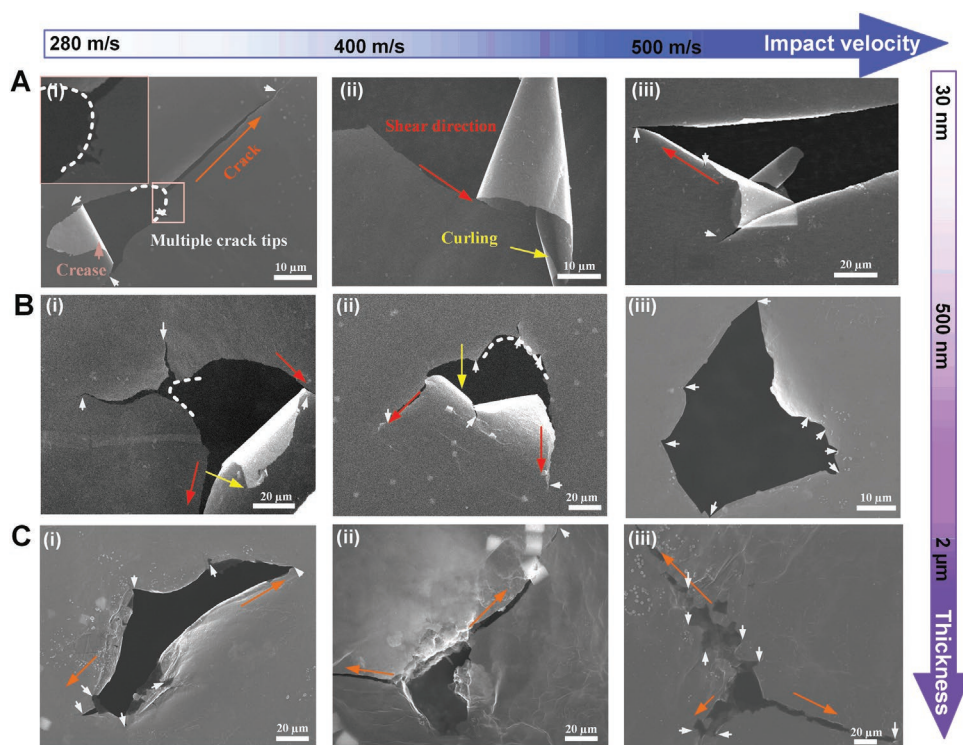
Figure 3. Post-mortem failure characteristics of the MLGDY films with different thicknesses at various impact velocities (V_i). a–c) Post-impact characteristics of the MLGDY films with thicknesses of 30 or 500 nm or 2 μm at V_i values of 280–500 m s^{-1}, as shown from left to right, respectively.

periphery at 280 and 400 m s^{-1} (Figure 3b-i,ii). At 500 m s^{-1}, the impact-induced petal detaches from the MLGDY target and an irregularly shaped perforation hole is formed (Figure 3b-iii; Figure S6b-ii, Supporting Information). With an increase in the thickness of MLGDY, the enhancement of the perforation area reverses, *i.e.*, the S_p values of the MLGDY films with thicknesses of 500 nm or 2 μm decrease with increasing V_i (Figure S7, Supporting Information). As thicker films display relatively strong support bases around the central impact areas, an increase in thickness limits the delocalized failure of the MLGDY film, particularly at a higher V_i. The relatively small perforation area and localized failure at a high V_i are significant reasons for the relatively low E_p^* of the thick MLGDY film.

With a further increase in the thickness of the MLGDY film to 2 μm, the tearing and curling of the petals, as observed in the films with thicknesses of 30 or 500 nm, become difficult. The two main radial cracks initiate and propagate along the direction of 45° at V_i = 280 m s^{-1} because of the inertia of material deformation due to the increased stiffness of the film (Figure 3c). The severe out-of-plane deformation of the material close to the crack surface during impact leads to a relatively large S_p (Figure S7, Supporting Information). When V_i is increased to 400 m s^{-1}, the impact region detaches completely from the MLGDY film, and three main directions of radial crack propagation are observed (Figure 3c-ii). S_p decreases drastically, indicating that a larger V_i hinders the expansion of S_p. At 500 m s^{-1}, the lengths of the cracks increase drastically compared to those observed at 280 and 400 m s^{-1}, whereas the width of the perforation hole, which is close to the diameter of the projectile, hardly changes, indicating the limited conical

deformation of the MLGDY film with a thickness of 2 μm (Figure 3c-iii; Figure S6, Supporting Information). Notably, the effect of the blast wave, which is produced during the launch process, on the post-penetration features of the MLGDY film may be neglected because the distance between the launch pad and target is sufficiently large, i.e., 1.3 cm (see Figure S3, Supporting Information).

Although it is a GR allotrope, the failure characteristics of the MLGDY films with thicknesses of 500 nm differ from those of MLGR films with identical thicknesses (Figure S8, Supporting Information). "Petal-like" failure characteristics, as observed by Lee et al.,[14] are manifested and extended along the direction of ≈120° in the MLGR films (Figure S8, Supporting Information) under the impact conditions, behaving more regularly than the MLGDY film. In contrast, the MLGDY film exhibits multiple crack tips, including the mainly propagated and minor crack tips (as indicated by the white arrows shown in Figure 3). During impact with the spherical microprojectile, owing to the anisotropic feature of the MLGDY film, the main radial crack initiates and propagates along the relatively weak diyne linkages, as indicated by the main directions of crack propagation (Figure 3). The diyne linkages are mainly responsible for the energy dissipation capacity during impact.[23] The multiple crack tips of the MLGDY film indicate multiple possible directions of crack propagation, further promoting energy dissipation. This also renders the MLGDY film a more designable alternative for use in impact resistance structures and composite materials by combining the ultra-high strength of GR with the low density and excellent toughness of GDY to realize a great mechanical performance in the near future.
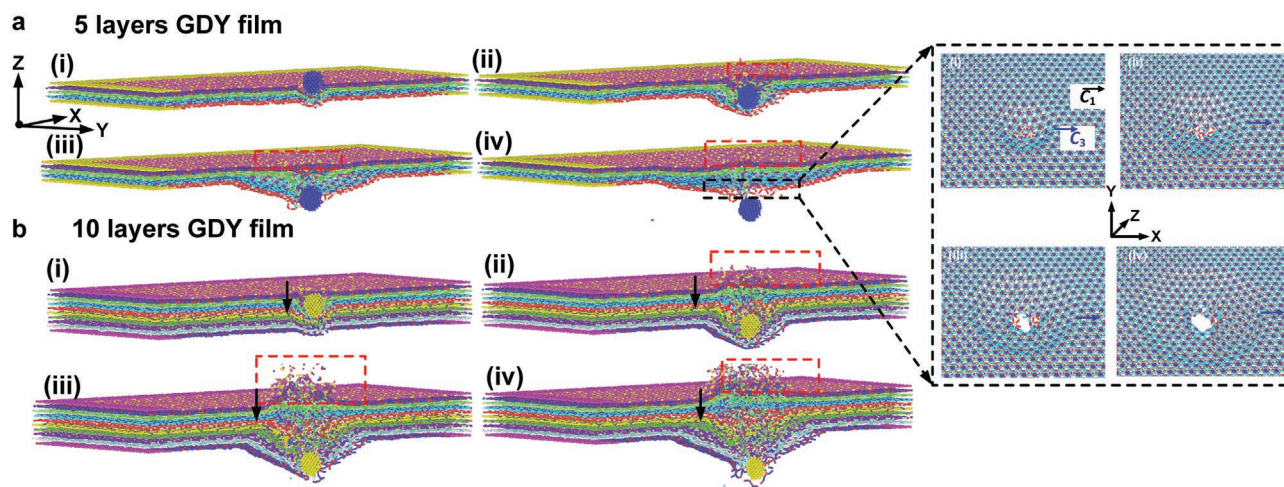
Figure 4. a) Failure morphologies of the 5-layer GDY film at i) 0.5, ii) 1.25, iii) 2.5, and iv) 3.75 ps at the ballistic limit (V_{50}) of 5.8 km s^{-1}. b) Failure morphologies of the 10-layer GDY film at i) 0.3, ii) 1.1, iii) 1.7, and iv) 2.2 ps at the V_{50} of 8.7 km s^{-1}.

2.4. Atomic-Scale Failure Features and Impact Resistance

MD simulations were performed to observe the dynamic deformation and failure behavior of the MLGDY film, explaining the ballistic resistance of the thickness-dependent behavior, and providing insightful strategies to further improve the impact resistances of these films (Figures S9 and S10, Supporting Information). Snapshots of 5- and 10-layer MLGDY films were investigated to reveal their dynamic deformation processes (see Supporting Information; **Figure 4**a,b).

The 5- and 10-layer MLGDY films were used as examples to analyze the thickness-dependent deformation behaviors and energy dissipation mechanisms. Continuous failure occurs from top to bottom during high-velocity ballistic impact (Figure 4a-i,b-i). In the 5-layer MLGDY film (Figure 4a), after the localized failure of the top layer, the compression stress attenuates and continues to propagate downward with a reduced amplitude, causing the subsequent deformation of the film. The velocity of the projectile declines sharply during the subsequent penetration of the remaining layers. The out-of-plane deformation coupled with the in-plane shock wave propagation facilitates the impact of energy dissipation. The entire film bears the impact-induced tensile force, effectively inducing delocalized deformation and promoting energy dissipation (Figure 4a-ii,iii). The large kinetic energy enables penetration (Figure 4a-iv,b-iv), and the side view of the bottom two layers of MLGDY also reveals in-plane stress ($C_1 \approx 20.78$ km s^{-1}) and conical wave propagation ($C_3 \approx 4$ km s^{-1}) at the atomic level (as indicated by the black-dotted box and arrows).[14]

In the 10-layer MLGDY film (Figure 4b), the sequence of the impact process suggests the presence of a thickness threshold that divides the system into upper and lower layers, depending on the deformation mode. The upper layers mainly undergo compression and shear deformation, causing delamination failure, which hinders energy dissipation via delocalized deformation. The lower layers (as indicated by the black arrows) mainly undergo impact-induced tension and effectively dissipate the impact energy. The threshold thickness for the change in the deformation mode should depend on V_i and the

structure of the material. This observation, *i.e.*, several upper layers of the MLGDY film display lower contributions to energy dissipation, may explain the experimentally observed lower E_p^* of the thicker film.

Compression wave propagation and a rarefaction wave at the upper free surface result in the characteristics of a bulging rim (Figure 4a-ii,iii-b-ii, and b-iii, as indicated by the red-dotted box), and stronger compression waves at a higher V_i cause a higher bulging rim. Moreover, a large conical out-of-plane deformation is caused by transverse wave propagation. In the MLGDY film, the failure morphology develops from a perforation hole, with a shape similar to that of the projectile, to a zigzag crack boundary, as observed experimentally, which differs from the MLGR system in forming clear petal-like damage (Figure S11a,b, Supporting Information). This wave-induced failure is generally related to the failure strength and intrinsic structure of the material. In MLGDY, the complex sp²- and sp-hybridized carbon atoms in GDY render its fracture feature similar to the structure of a rope network, and the final annular perforation hole is formed.[16c] The crack propagates in the target along the directions with relatively low binding energies owing to bond cleavage, further contributing to the impact energy. In GR, sp²-hybridized carbon atoms yield a typical damage morphology of asymmetrically shaped petals with different radial angles. The abundant zigzag crack initiation and propagation at the boundary of the perforation hole are critical in the energy dissipation of the MLGDY film after failure.

Notably, perforation failure in the MD simulations did not reproduce the shear failure observed experimentally. The different perforation failure behaviors observed in the experiments and simulations originated from two aspects. The system energy was not precisely conserved, as the number of layers increased once the cut-off radius of the adaptive intermolecular reactive empirical bond-order potential was modified to 2.0 Å. However, this modification was necessary to study the dynamic performances of the MLGDY films. On the other hand, the highest experimental V_i was 500 m s^{-1} (strain rate of $\approx 10^6$ s^{-1}), whereas it was several kilometers per second in the MD simulations (strain rate of $\approx 10^8$–10^{10} s^{-1}). The relatively
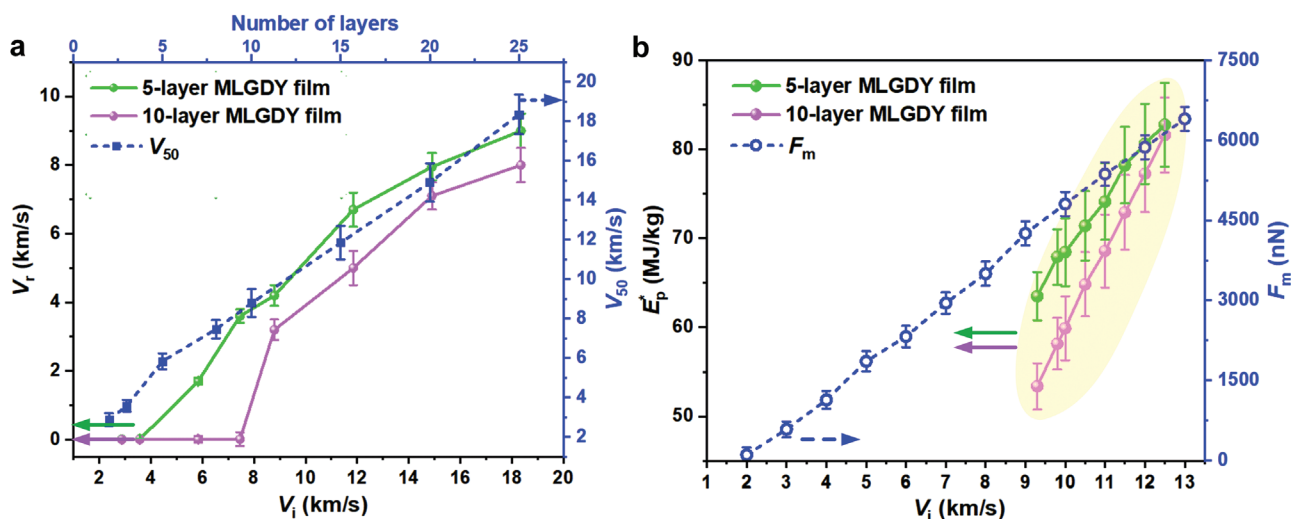
Figure 5. a) Relationships between V_i and V_r of the 5- and 10-layer MLGDY films, and the almost linear relationship between V_{50} and the number of GDY layers impacted by a projectile. b) Specific penetration energies (E_p^*) of the 5- and 10-layer MLGDY films impacted by projectile with diameter of 2 nm and the linear relationship between the maximum force of the projectile (F_m) and V_i for the 10-layer GDY film.

high strain rate in the MD simulations also caused atomic scattering during penetration. Although a difference in perforation failure compared with that observed experimentally was apparent, the MD-simulated dynamic deformation, failure behavior, and interaction between layers could still explain the experimentally observed ballistic resistance of the thickness-dependent behavior. Also, it is challenging to reproduce the experimental conditions in MD simulation, especially for relatively thick MLGDY film, due to the limitation of computation scale and efficiency.

The relationships between V_r and V_i of the 5- and 10-layer MLGDY and MLGR films were obtained (**Figure 5**a; Figure S12a, Supporting Information) via extensive calculations. When V_i is slower than the ballistic limit V_{50}, V_r is close to zero, and the projectile is captured by the target. At $V_i > V_{50}$, V_r becomes positive and increases with V_i, and an inelastic conical deformation with a perforation hole occurs, which dissipates the impact energy via deformation and crack propagation.

The relationship between V_{50} and the number of layers is also plotted (Figure 5a). With increasing film thickness, the V_{50} values of the MLGDY and MLGR films increase almost linearly. In the simulations, the thickness (h) of the MLGDY film changes from 0.7 to 9.13 nm, corresponding to an increase from 2 to 25 layers. The ratio of the thickness of the MLGDY film to the projectile diameter (2 nm) is >0.2, and thus, the impact event can be regarded as a thin-plate ballistic impact. This displays more complex mechanisms, including spall and radial fracture, petaling, plugging, and ductile hole enlargement,[24] during impact. This is due to the significant influence of the internal wave-induced overall deformation in the thickness direction compared to that of a thin-film ballistic impact. A similar phenomenon is observed in the MLGR film (Figure S12a, Supporting Information).

The E_p^* values of the 5- and 10-layer MLGDY films at V_i = 9.3 km s^{-1} are ≈64 and 53 MJ kg^{-1} (Figure 5b), respectively, indicating energy dissipation capacities comparable to that of the MLGR film (Figure S12b, Supporting Information).

Such a low-density material with a high E_p^* may be characterized by extremely fast stress wave, plastic deformation, and crack propagation. In addition, E_p^* decreases as the thickness of the MLGDY film increases, which is consistent with the experimental results and may be explained by the change in deformation mode. Notably, E_p^* is calculated only when perforation occurs, and the maximum resistance forces (F_m) of the 10-layer MLGDY films were determined at different V_i values from non-perforation to perforation to analyze their impact resistances (Figure 5b). Notably, multiple peaks are observed in the force–time curve of the projectile (Figure S13, Supporting Information) at a low V_i. Therefore, we use the first peak as F_m because it always represents the maximum force, even if the projectile is captured by the target. Remarkably, the F_m values of the MLGDY and MLGR films increase linearly with increasing V_i (Figure S12b, Supporting Information). Generally, the compression resistances of fiber-reinforced laminates under macroscopic ballistic impact may be expressed empirically as $\sigma = \sigma_e + \beta V_i \sqrt{\rho_l \sigma_e}$, where σ is the intensity of the stress wave during impact, σ_e is the linear elastic limit strength when the laminate is compressed in the thickness direction, which is related to the elastic compressive modulus of the laminate, ρ_l is the density of the laminate, and β is an empirical constant. Thus, the intensity of the stress wave is linearly related to V_i and determined by the density and elastic limit strength of the fiber-reinforced laminate. The linear relationships between F_m and V_i of the MLGDY and MLGR films, as observed in this study, indicate that the empirical relationship for macroscopic ballistic impact is still applicable for nanosystems.[25] Increasing the compression strength should yield a higher F_m. Therefore, the compression strengths of the MLGDY films may be further improved by combining them with high-strength GR films or rotating the interlayer of MLGDY to avoid the direct stacking of sp-hybridized carbon atoms to realize an even higher impact resistance (Figure S14b, Supporting Information).

A preliminary simulation of the effects of rotation schemes on the dynamic performance of the 5-layer MLGDY film was

**ADVANCED
SCIENCE NEWS**

www.advancedsciencenews.com

**ADVANCED
FUNCTIONAL
MATERIALS**

www.afm-journal.de

also performed (see Figure S15, Supporting Information). Three rotation schemes of MD models, denoted Models (ii)–(iv), were investigated relative to the direct stacking model, *i.e.*, stacking sequences of [0/2/4/6/8], [0/5/10/-10/-5], and [0/15/30/60/90]. The rotation axis is along the *z*-axis of the model, and a positive angle represents anticlockwise rotation. The observed E_p^* indicates an improvement of ≈5% compared to the direct stacking model. Notably, the E_p^* values of Models (ii)–(iv) are almost identical, indicating that the stacking angles of these rotation schemes do not affect the impact resistance of MLGDY film, which is similar to that of the GR film.[26] Further careful studies regarding the optimal number of layers and rotation angle shall be conducted in the near future.

3. Conclusion

In summary, the dynamic thickness-dependent performances of MLGDY films were investigated using LIPIT and MD simulations, which provided an understanding of the use of such a multi-nano-walled ultralight film as an effective energy dissipation material in anti-micro-ballistic impact applications. The excellent in-plane wave velocity and multiple crack initiation and propagation due to the introduction of diacetylene linkages between the benzene rings endowed MLGDY with an excellent energy dissipation capacity. Failure characteristics, such as clear creasing, curling, and shear failure, also contributed to the impact resistance of MLGDY. The E_p^* of the MLGDY film decreased with increasing thickness, which could be explained by the deformation modes during micro-ballistic impact. In a relatively thick MLGDY film, delamination failure of several upper layers occurred due to compression-shear deformation, which hindered the delocalized energy dissipation capacity and thus decreased the impact resistance of the film. In addition, F_m increased linearly with increasing V_i, indicating the applicability of the macroscopic ballistic impact theory of laminates to nanoscopic films. Furthermore, two viable fabrication strategies, *i.e.*, combination with high-strength multilayer GR or rotating interlayer GDY to avoid the direct stacking of sp-hybridized carbon atoms, are proposed to further improve the impact resistances of MLGDY films. Our results indicate the considerable potential of MLGDY films for use in designing composite materials with excellent impact resistances.

4. Experimental Section

Materials: The GDY films were synthesized using a previously described method.[7a,27] Copper foil was pretreated via sonication in 3 M HCl, water, and ethanol for 5 min, dried under a flow of nitrogen gas, and then used immediately in GDY film formation. The treated copper plates were added to a mixture of acetone, pyridine, and tetramethylethylenediamine in a volume ratio of 100:5:1 in a flask. A hexaethynylbenzene (HEB) monomer was synthesized in good yield (62%) by adding tetrabutylammonium fluoride to a solution of hexakis[(trimethylsilyl)ethynyl]benzene in tetrahydrofuran, which was then stirred for 10 min at 0 °C. Subsequently, HEB was dissolved in acetone, added slowly over 3 h to the mixture containing the copper plates, and maintained under an argon atmosphere at 60 °C for 24 h. The GDY films then formed on the surface of the copper foil, and the copper plates were washed with hot acetone and dimethylformamide to

remove the unreacted monomer and oligomer and dried under ambient nitrogen. After the preparation of the GDY films, a 1 M iron chloride solution was used to exfoliate the MLGDY film from the copper substrate and suspend the film. This solution was replaced with secondary water until it became clear (Figure S1, Supporting Information). Subsequently, a liquid adhesive polymer (Scotch Super 77, 3M, Saint Paul, MN, USA) was diluted in toluene to a concentration of ≈20 wt.%, and this solution was dropped onto a copper TEM grid to coat the grid frame with the non-water-soluble adhesive.[14,28]

To prevent the sticky polymer solvent from blocking the pores of the TEM grid, air was blown through the grid holes from one side. The suspended MLGDY film was then mounted on the preprocessed TEM grid on the side with the adhesive. Subsequently, the MLGDY film with the designed thickness adhered to the TEM grid, which was then dried in a vacuum at 40 °C for 30 h prior to LIPIT. The MLGR film with a thickness of 500 nm was obtained via the mechanical exfoliation of highly ordered pyrolytic graphite, and the preparation process was very similar to that used to prepare the MLGDY film.

Material Characterization: The chemical compositions of the prepared MLGDY films were analyzed via XPS (ESCALab 2201-XL, VG Scientific, Waltham, MA, USA), and Raman spectroscopy was conducted using a confocal Raman microscope (LabRAM HR Evolution, Horiba, Kyoto, Japan) with argon laser excitation at 473 nm. The morphological features and failure characteristics of the MLGDY and MLGR films were analyzed using field-emission SEM (S-4800, Hitachi, Tokyo, Japan), and the thicknesses of the MLGDY films with thicknesses of 500 nm or 2 μm were measured using FIB-SEM (Scios 2 DualBeam, Thermo Fisher Scientific, Waltham, MA, USA). The interlayer spacing of the MLGDY film was measured using TEM (JEM-2100Plus, JEOL, Tokyo, Japan) at 200 kV, and the surface roughness and morphologies of the MLGDY films were investigated using AFM (Multimode 8, Bruker, Billerica, MA, USA).

Projectile and Launch Pad Preparation: A cluster of silica projectiles with diameters of 25 μm was dispersed in 20 mL ethanol and then ultrasonicated for 10 min. The launch pad was fabricated as described by Lee et al.[14] and Hyon et al.[18] K9 glass with a diameter of 25.4 mm was first coated with a gold film with a thickness of 30 nm using a magnetron sputtering coater (PVD 75, Kurt J. Lesker, Jefferson Hills, PA, USA). Subsequently, a polydimethylsiloxane (PDMS) solution was prepared using a two-part PDMS kit (Sylgard 184, Dow, Midland, MI, USA), consisting of a PDMS monomer solution and PDMS hardener, which were mixed in a 10:1 mass ratio and allowed to settle for 1 h. The gold/glass component was then coated with the PDMS solution via spin coating, yielding a PDMS top film with a thickness of 40 μm. The launch pad was then placed under vacuum for 1 h and thermally cured for 24 h at 60 °C. The prepared projectile with a diameter of 25 μm was dropped onto the launch pad, and a standard lab wipe (Kimwipes, Kimberly-Clark, Irving, TX, USA) was used to spread the projectile on the surface of the PDMS film.

Fabrication of Numerical Samples: The GDY structure includes three types of bonds, i.e., single, aromatic (e.g., sp^2), and triple (i.e., sp), and the original bond lengths of the single, aromatic, and triple bonds were set as 1.40, 1.44, and 1.24 Å, respectively. However, the GR model includes only one bond type, with the length set as 1.42 Å, based on previous studies.[29] The MD-simulated models of several layers of GDY and GR were established using the atomic coordinates (Figures S9 and S10, Supporting Information). The elastic moduli, strengths, and fracture features of GDY and GR were efficiently captured to confirm the computational models.[13,30] A spherical projectile with a diamond structure (sp^3-hybridized carbon atoms) was constructed and considered as a rigid object during impact, and the diameter of the projectile was set as 2 nm. In addition, the projectile was located at the central position of the X-Y plane in the simulated system and 20 Å from the MLGDY and MLGR films in the Z direction to avoid initial interactions prior to impact.

Software Used: The perforation area and largest length of the perforation hole were measured using ImageJ 1.53f51 (National Institutes of Health, Bethesda, MD, USA), and all MD simulations were

performed using the large-scale atomic/molecular massively parallel simulator code.[31] The open-source visualization software OVITO[32] (OVITO, Darmstadt, Germany) was used to visualize the atomic configurations during impact.

Statistical Analysis: Each measured thickness of the MLGDY film was the average of seven measurements. Each V_i in LIPIT was used four times to calculate E_p^*. To obtain the V_{50} values of the MLGDY films with different numbers of layers, the MD-simulated impact was repeated ten times at each V_i with a random seed configuration for each layer. V_i was defined as V_{50} if the MLGDY film penetration probability was 50%. Error bars of experimental data were presented as mean ± standard deviation, and Microsoft Excel (Microsoft, Redmond, WA, USA) was used to calculate the error of each simulation.

Supporting Information

Supporting Information is available from the Wiley Online Library or from the author.

Acknowledgements

Conflict of Interest

The authors declare no conflict of interest.

Data Availability Statement

The data that support the findings of this study are available from the corresponding author upon reasonable request.

Keywords

[1] B. Li, C. Lai, M. Zhang, G. Zeng, S. Liu, D. Huang, L. Qin, X. Liu, H. Yi, F. Xu, N. An, L. Chen, *Adv. Energy Mater.* **2020**, *10*, 2000177.

[2] a) D. Berman, A. Erdemir, A. V. Sumant, *Appl. Phys. Lett.* **2014**, *105*, 231907; b) S. Blankenburg, M. Bieri, R. Fasel, K. Muellen, C. A. Pignedoli, D. Passerone, *Small* **2010**, *6*, 2266; c) X. Chen, P. Gao, L. Guo, S. Zhang, *Sci. Rep.* **2015**, *5*, 16720; d) H. Du, H. Yang, C. Huang, J. He, H. Liu, Y. Li, *Nano Energy* **2016**, *22*, 615; e) H. Tian, B. Zhang, Q. M. Li, *Mech. Mater.* **2019**, *133*, 1.

[3] a) N. Wang, J. He, K. Wang, Y. Zhao, T. Jiu, C. Huang, Y. Li, *Adv. Mater.* **2019**, *31*, 1803202; b) F. Xu, K. Meng, B. Zhu, H. Liu, J. Xu, J. Yu, *Adv. Funct. Mater.* **2019**, *29*, 1904256.

[4] a) L. Li, Z. Zuo, F. Wang, J. Gao, A. Cao, F. He, Y. Li, *Adv. Mater.* **2020**, *32*, 2000140; b) R. Ding, W. Li, X. Wang, T. Gui, B. Li, P. Han,

[5] H. Tian, A. Liu, X. Wang, X. Liu, X. Gao, W. Wang, L. Song, *J. Alloys Compd.* **2018**, *764*, 1039; c) Y. Liu, Y. Xue, H. Yu, L. Hui, B. Huang, Y. Li, *Adv. Funct. Mater.* **2021**, *31*, 2010112.

[5] a) J. D. Roy-Mayhew, I. A. Aksay, *Chem. Rev.* **2014**, *114*, 6323; b) Z. Jin, M. Yuan, H. Li, H. Yang, Q. Zhou, H. Liu, X. Lan, M. Liu, J. Wang, E. H. Sargent, Y. Li, *Adv. Funct. Mater.* **2016**, *26*, 5284.

[6] N. B. Baghbani, J. Azamat, H. Erfan-Niya, S. Majidi, L. Khazini, *J. Mol. Graph. Model.* **2020**, *101*, 107729.

[7] a) Q. Chang, F. Wang, Z. Zuo, F. He, Y. Zhao, F. Wang, Y. J. S. Li, *Small* **2021**, *17*, 2102066; b) J. Li, Y. Chen, J. Guo, F. Wang, H. Liu, Y. Li, *Adv. Funct. Mater.* **2020**, *30*, 2004115.

[8] L. Hui, Y. Xue, Y. Liu, Y. Li, *Small* **2021**, *17*, 2006136.

[9] a) Y. Kong, X. Li, L. Wang, Z. Zhang, X. Feng, J. Liu, C. Chen, L. Tong, J. Zhang, *ACS Nano* **2022**, *16*, 11338; b) Z. Zhu, Q. Bai, S. Li, S. Li, M. Liu, F. Du, N. Sui, W. W. Yu, *Small* **2020**, *16*, 2001440.

[10] X. Gao, H. Liu, D. Wang, J. Zhang, *Chem. Soc. Rev.* **2019**, *48*, 908.

[11] G. Li, Y. Li, H. Liu, Y. Guo, Y. Li, D. Zhu, *Chem. Commun.* **2010**, *46*, 3256.

[12] a) R. E. Roman, S. W. Cranford, *Adv. Eng. Mater.* **2014**, *16*, 862; b) S. W. Cranford, D. B. Brommer, M. J. Buehler, *Nanoscale* **2012**, *4*, 7797; c) S. W. Cranford, M. J. Buehler, *Carbon* **2011**, *49*, 4111.

[13] K. Xiao, J. Li, X. Wu, H. Liu, C. Huang, Y. Li, *Carbon* **2019**, *144*, 72.

[14] J. H. Lee, P. E. Loya, J. Lou, E. L. Thomas, *Science* **2014**, *346*, 1092.

[15] M. G. Ahangari, *Physica E* **2015**, *66*, 140.

[16] a) K. Xia, H. Zhan, X. Zhang, Z. Li, *Mater. Res. Express* **2020**, *7*, 115602; b) Y. Yang, Q. Cao, Y. Gao, S. Lei, S. Liu, Q. Peng, *RSC Adv.* **2020**, *10*, 1697; c) K. Xiao, Q. Yin, X. Wu, C. Huang, *Nano Mater. Sci.* **2022**, *4*, 383.

[17] a) J. Li, X. Gao, B. Liu, Q. Feng, X. B. Li, M. Y. Huang, Z. Liu, J. Zhang, C. H. Tung, L. Z. Wu, *J. Am. Chem. Soc.* **2016**, *138*, 3954; b) J. He, N. Wang, Z. Cui, H. Du, L. Fu, C. Huang, Z. Yang, X. Shen, Y. Yi, Z. Tu, Y. Li, *Nat. Commun.* **2017**, *8*, 1172.

[18] J. Hyon, O. Lawal, O. Fried, R. Thevamaran, S. Yazdi, M. Zhou, D. Veysset, S. E. Kooi, Y. Jiao, M.-S. Hsiao, J. Streit, R. A. Vaia, E. L. Thomas, *Mater. Today* **2018**, *21*, 817.

[19] J. Hyon, M. Gonzales, J. K. Streit, O. Fried, O. Lawal, Y. Jiao, L. F. Drummy, E. L. Thomas, R. A. Vaia, *ACS Nano* **2021**, *15*, 2439.

[20] a) C. Lee, X. Wei, J. W. Kysar, J. Hone, *Science* **2008**, *321*, 385; b) C. Lee, X. Wei, Q. Li, R. Carpick, J. W. Kysar, J. Hone, *Phys. Status Solidi B* **2009**, *246*, 2562.

[21] J. Cai, R. Thevamaran, *Nano Lett.* **2020**, *20*, 5632.

[22] E. P. Chan, W. Xie, S. V. Orski, J.-H. Lee, C. L. Soles, *ACS Macro Lett.* **2019**, *8*, 806.

[23] J. C. Newman, *Int. J. Fract.* **1984**, *24*, R131.

[24] A. Shahkarami, E. Cepus, R. Vaziri, A. Poursartip, in *Lightweight Ballistic Composites* (Ed: A. Bhatnagar), Woodhead Publishing, Cambridge **2006**.

[25] a) Z. Meng, J. Han, X. Qin, Y. Zhang, O. Balogun, S. Keten, *Carbon* **2018**, *126*, 611; b) T. He, H. M. Wen, Y. Qin, *Compos. Struct.* **2007**, *81*, 243; c) Q. G. Wu, H. M. Wen, Y. Qin, S. H. Xin, *Compos. Part B-Eng.* **2012**, *43*, 221.

[26] X. Yang, B. Zhang, *Appl. Surf. Sci.* **2021**, *538*, 148030.

[27] a) G. Li, Y. Li, H. Liu, Y. Guo, Y. Li, D. Zhu, *Chem. Commun.* **2010**, *46*, 3256; b) J. Zhou, X. Gao, R. Liu, Z. Xie, J. Yang, S. Zhang, G. Zhang, H. Liu, Y. Li, J. Zhang, Z. Liu, *J. Am. Chem. Soc.* **2015**, *137*, 7596.

[28] J. Hyon, O. Lawal, R. Thevamaran, Y. E. Song, E. L. Thomas, *Adv. Sci.* **2021**, *8*, 2003142.

[29] a) W. Wang, C. Yi, X. Ji, X. Niu, *Nanosci. Nanotechnol. Lett.* **2012**, *4*, 1188; b) Y. Gao, P. Hao, *Physica E* **2009**, *41*, 1561.

[30] Y. Lin, L. Tong, *Carbon* **2016**, *107*, 689.

[31] S. Plimpton, *J. Comput. Phys.* **1995**, *117*, 1.

[32] L. A. Zepedaruiz, A. Stukowski, T. Oppelstrup, V. V. Bulatov, *Nature* **2017**, *550*, 492.